PERGAMON

International Journal of Solids and Structures 39 (2002) 1077–1096

INTERNATIONAL JOURNAL OF SOLIDS and STRUCTURES

www.elsevier.com/locate/ijsolstr

Modeling of the metal powder compaction process using the cap model. Part II: Numerical implementation and practical applications

Hédi Chtourou [a,b,c], Augustin Gakwaya [a,c,*], Michel Guillot [a,c]

[a] *P/M Laboratory—Précitech Inc. and Université Laval, Que., Canada G1P 4P4*
[b] *Department of Technology, IPEIS, Sfax University, Tunisia*
[c] *Department of Mechanical Engineering, Laval University, Pavillon Pouliot, Sainte Foy, Que., Canada G1K 7P4*

Received 2 August 1997

Abstract

The finite element (FE) simulation method has recently been used as an alternative design tool in powder metallurgy (PM) industry. It allows for the prediction of density and stress distributions in the pressed compact prior to the actual tooling design and manufacturing activity. It thus makes possible the validation of the PM part and associated tooling design. However, the accuracy of FE prediction highly depends on the choice of an appropriate and well calibrated powder material model, as well as on the effectiveness of the computational environment. While the first point was presented in a previous work, the present paper addresses some computational aspects of compaction process modeling approach in the context of industrial production environment.

Hence, this paper presents a discussion of the choice of stress and strain measures used in this large deformation context. It also presents the implementation of the cap constitutive model into ABAQUS FE software using the closest point projection algorithm. Furthermore, an integrated simulation module has been developed and is described herein. This module, designed in order to render the modeling approach practical and industrially attractive to PM engineers, permits an easy definition of the tooling and the powder geometry, as well as the prescription of compaction sequence and all other boundary conditions.

Finally, the simulation of the compaction of an industrial PM part, intended to illustrate the usefulness of the simulation approach in the task of improving the design of PM part and process, is presented. © 2002 Published by Elsevier Science Ltd.

Keywords: Powder metallurgy; Finite element simulation; Constitutive model nonlinearity; Friction; Cap model; Numerical integration; Closest point projection; Algorithmic consistency

* Corresponding author. Address: Department of Mechanical Engineering, Laval University, Pavillon Pouliot, Sainte Foy, Que., Canada G1K 7P4. Tel.: +1-418-656-5548; fax: +1-418-656-7415.

E-mail address: agakwaya@gmc.ulaval.ca (A. Gakwaya).

0020-7683/02/$ - see front matter © 2002 Published by Elsevier Science Ltd.
PII: S0020-7683(01)00256-6

1. Introduction

Due to its numerous technological and economic advantages, powder metallurgy (PM) is a fast evolving manufacturing process (Lenel, 1980). However, due to the complex powder deformation mechanisms occurring during the compaction process, density gradients are often present in pressed parts (Bockstiegel, 1968). These gradients are the main causes of part distortion during the subsequent process of sintering and may even lead to part fracture during its ejection from the compaction die. Thus, part and tooling design is a very delicate task. Except for routine parts, for which PM engineers have developed extensive know-how, this task is traditionally performed through expensive trial and error approach. Thus, more efficient alternatives are still to be settled.

Therefore, the finite element (FE) simulation method has recently been used as such an alternative design tool in PM industry. It allows for the prediction of density and stress distributions in the pressed compact prior to the actual tooling design and manufacturing activity. It thus makes possible the validation of the PM part and associated tooling design (German, 1984). However, the accuracy of FE prediction highly depends on the choice of an appropriate and well calibrated powder material model, as well as on the effectiveness of the computational environment. In fact, in order to correctly model the compaction problem, such an environment should permit a reliable and practical representation of the model boundary conditions and should adequately handle the three involved nonlinearities, i.e.: the geometric nonlinearity associated with the large displacements, the material nonlinearity related to the elastic–plastic behavior of the powder material and finally, the contact nonlinearity related to friction between tools and powder.

In a previous paper (Chtourou et al., 2001), the cap material model, traditionally used for hard and nonductile powder was chosen and adapted for metal powders. The same paper presented an experimental calibration methodology and its application for the case of 316L stainless steel powders, as well as an experimental procedure for the validation of the model simulation results.

The present paper addresses some computational aspects of compaction process modeling approach in the context of industrial production environment. First, we justify the choice of stress and strain measures used in this large deformation context and we succinctly present the basic equations of the cap material model. Then, we present the integration algorithm used to implement the cap model in ABAQUS FE software through the user's material subroutine. Subsequently, in order to render this modeling approach practical and industrially attractive to PM engineers, an integrated simulation module has been developed and is described herein. This module permits an easy definition of the tooling and the powder geometry, as well as the prescription of compaction sequence and all other boundary conditions. It also handles FE solution and result post-processing. Finally, the simulation of the compaction of an industrial PM part, intended to illustrate the usefulness of the simulation approach in the task of improving the design of PM part and process, is presented.

2. Material modeling

2.1. Strain and stress measures

Let $\mathrm{B} \in \mathfrak{R}^n$, $n = 2,3$ and $B_t = \phi_t(B)$ be respectively the reference and the current configuration of the body under consideration and where function ϕ_t maps reference points X of B onto current points $x = \phi_t(X) \in B_t$, i.e. ϕ_t describes the deformational motion of body B. We also introduce a time like interval $[0, T]$ such that $t \in [0, T]$ is to be understood as a monotonically increasing parameter describing the evolution of the deformation process.

To describe the inelastic response in metal plasticity applications, we follow Kröner (1960), Lee and Liu (1967) or Mandel (1971) and introduce the multiplicative split of the deformation gradient, $F(X) = \partial\phi_t(X)/\partial X$, into elastic part F^e and plastic part F^p:

$$F(X,t) = F^e(X,t)F^p(X,t) \tag{1}$$

An appropriate definition of strain rate is then be introduced by considering the spatial velocity gradient l which is then expressed as

$$l = \dot{F}\cdot F^{-1} = \dot{F}^e\cdot F^{e^{-1}} + F^e\cdot(\dot{F}^p\cdot F^{p^{-1}})\cdot F^{e^{-1}} = l^e + F^e\cdot(l^p)\cdot F^{e^{-1}} \tag{2}$$

Using the polar decomposition of F^e into the elastic rotation tensor R^e and the left stretch tensor V^e (i.e.: $F^e = V^e\cdot R^e$) and assuming, as usual for most metals undergoing large deformation, that the elastic strain is negligible compared to the plastic strain, it is then reasonable to consider the elastic stretch tensor V^e to be given by $V^e = \mathbf{I} + \varepsilon^e$ where ε^e is the infinitesimal elastic strain tensor. Following Lee and Liu (1967), we take $F^e = V^e$ and by neglecting higher order infinitesimal quantities, one can arrive at the usual approximation of metal plasticity (Eq. (3)), where sym[·] denotes the symmetric part of a tensor and where d, d^e and d^p denote respectively the total, the elastic and the inelastic strain rate tensors.

$$\mathrm{sym}[l] = d \cong d^e + d^p \tag{3}$$

As a stress measure, we consider, the Kirchoff stress tensor τ which is an energy conjugate stress measure associated with d. Hence, the rate of internal work in the current configuration will be written as: $\dot{W}_{\mathrm{int}} = \int_{B_t}(\tau\cdot d)\mathrm{d}v$ (Peric et al., 1992; Simo, 1992; Simo and Ortiz, 1985). However, since the elastic strains are very small, it is common to approximate the Kirchoff stress by the true Cauchy stress since these two tensors are related by: $\tau = \det|F^e|\sigma$ (HKS, 1995b).

2.2. Cap material model

The cap model is a multisurface elastoplasticity permitting the representation of densification, hardening as well as inter-particle friction. It was originally developed for rocks, soils and other geological materials (Chtourou et al., 1995a; Chtourou et al., 1996; Dimaggio and Sandler, 1971). Due to the similarities in behavioral response of geological materials and some hard metal powders, this model was adopted and used to simulate the cold die compaction of tungsten carbide powder (Crawford and Lindskog, 1983; Weber and Brown, 1989). This kind of model was chosen in the present study because of the great flexibility it has shown in modeling all the compaction stages, especially the early ones (Trasorras et al., 1989). Provided some adjustments are performed (Weber and Brown, 1989; Gurson and Posteraro, 1992), this model is suitable for the simulation of the compaction of ductile powders able to attain higher density ranges. Box 1 succinctly presents the main features of the cap model in terms of J_1, the stress first invariant, and of s, the norm of the stress deviator $\mathbf{S}$ defined by $\mathbf{S} = \boldsymbol{\sigma} - (J_1/3)\mathbf{1}$ (Dimaggio and Sandler, 1971; Trasorras et al., 1989; Sandler and Rubin, 1979; Chtourou et al., 1995b; Hofstetter et al. 1993).

Box 1. Summary of the used multisurface plasticity cap model for powder compaction.

1. Stress–strain relationship (Hyperelastic compressible granular solid):

$$\sigma = \overline{\mathbf{C}}\varepsilon^e = \overline{\mathbf{C}}(\varepsilon - \varepsilon^p) \quad \text{with } \overline{\mathbf{C}} = \frac{\partial^2\psi}{\partial\varepsilon^2} = 2G(\rho)\overline{\mathbf{I}} + \left(K(\rho) - \frac{2G(\rho)}{3}\right)\mathbf{1}\otimes\mathbf{1}$$

where ψ is an hyperelastic free energy, $\overline{\mathbf{C}}$ is the fourth order elasticity tensor, $\bar{\mathbf{I}}$ and $\mathbf{1}$ are respectively the fourth and second order identity tensors, G and K are the shear and bulk moduli expressed in terms of the powder relative density ρ.

2. *Multi-yield surface*

(a) Surface tension limit:

$$f_1(\sigma) = T - J_1 = 0 \quad \text{for } J_1 < -T$$

(b) Shear failure surface:

$$f_2(\sigma) = s - F_e(J_1) = 0 \quad \text{for } -T \leqslant J_1 \leqslant L(k)$$

with:

$$F_e(J_1) = \alpha - \gamma e^{-\beta J_1} + \theta J_1 \quad \text{and} \quad L(k) = \begin{cases} k & \text{if } k \succ 0 \\ 0 & \text{if } k \leqslant 0 \end{cases}$$

(c) Cap hardening surface:

$$f_3(\sigma, K) = F_c(J_1, s, k) - F_e(k) = 0 \quad \text{for } L(k) \leqslant J_1 \leqslant X(k)$$

with:

$$F_c(J_1, s, K) = \sqrt{s^2 - \frac{1}{R^2}[J_1 - L(k)]^2}$$

and variable aspect ratio:

$$R(\rho) = \frac{X(k) - k}{F_e(k)}$$

where k is the internal state variable representing material hardening whereas T, α, β, γ and θ are material parameters and $X(k)$ the intersection of the cap and J_1 axis.

3. *Evolution equations*

(a) Flow rule:

$$\dot{\varepsilon}^p = \sum_{i=1,3} \dot{\lambda}_i \frac{\partial f_i(\sigma, k)}{\partial \sigma}$$

(b) Hardening law:

$$\overline{\varepsilon}_v^p[X(k)] = W(1 - e^{-DX(k)}) \quad \text{with } \overline{\varepsilon}_v^p = \begin{cases} \varepsilon_v^p & \text{if } \dot{\varepsilon}_v^p \geqslant 0 \text{ or if } k > 0 \text{ and } k > J_1 \\ 0 & \text{otherwise} \end{cases}$$

(c) Updating of density:

$$\rho = \rho_0 e^{-\varepsilon_v^p}$$

where $\dot{\lambda}_i$ is the plastic consistency parameter associated with the yield surface function f_i, W and D are material parameters and ρ_0 is the initial loose state density.

3. Numerical implementation

3.1. Solution of the nonlinear finite element problem

The compaction process is assumed to be a quasi-static transformation with the final spatial distribution of density ($\rho(\mathbf{x})$) as the driving unknown (Weber and Brown, 1989; Trasorras et al., 1989; Koopman et al., 1992). Every material point undergoes finite strains deformation and elastoplastic transformations take place under the interaction of the powder medium and the tooling components. The corresponding nonlinear structural FE analysis involves integration of the differential elastoplastic equations in time and space. The time integration in the present context is due to the discretization of the loading history, while the spatial integration is normally performed via Gauss quadratures at the FE level and then assembled in terms of the mechanical degrees of freedom.

A nonlinear solver based on the Newton–Raphson method (HKS, 1995b; Dhatt and Touzot, 1984) has been used. This choice is motivated by the presence of strong nonlinearities and the desired quadratic rate of convergence. The used scheme thus required the updating of the consistent tangent stiffness at each iteration and the use of the algorithmic tangent material operator (Simo and Ortiz, 1985). Hence, at the end of each time step, the current stress state satisfies in the weak sense the equilibrium of the mechanical system with the external forces and complies with the full consistency of the elastoplastic material and frictional contact formulation.

3.2. Numerical integration of the cap model

At the core of the nonlinear FE solver resides the constitutive driver for integrating the rate form of the elastoplastic constitutive relations in a finite time step Δt between times t_n and t_{n+1}. The problem is thus formulated as follows: Given the initial data at an integration point $(\sigma_n, \varepsilon_n^{\mathrm{p}}, k_n)$ at time t_n, and assuming that we are also given the total strain increment $\Delta\varepsilon_{n+1}$ corresponding to the displacement values u_{n+1} (best iterative guess at current iteration), one must then obtain the new values of the state variables $(\sigma_{n+1}, \varepsilon_{n+1}^{\mathrm{p}}, k_{n+1})$ satisfying the yield criteria and deduce values of the dependent variables such as stresses τ_{n+1} at time t_{n+1} (Chorin et al., 1978). The incremental integration scheme is then a two-phase process that checks first whether plastic loading takes place by evaluating the yield function at the trial stress state (elastic prediction). In case of plastic loading, the flow direction and the magnitude of the incremental plastic multiplier are subsequently determined using full consistency at t_{n+1}.

The first numerical simulations using the cap model were based on the algorithm proposed by Sandler and Rubin (1979). This algorithm was found to be not fully consistent with the principles of plastic consistency and associativity of the flow rule and was then corrected for these limitations (Simo et al., 1988a). Hofstetter et al. (1993) have then proposed an improved formulation of the cap model yield functions in order to ensure a better numerical stability of the model. They also derived a consistent expression of an algorithmic elastoplastic tangent moduli which is required in order to preserve the quadratic rate of convergence in a Newton–Newton solution technique. An improvement and adaptation of the work of reference Hofstetter et al. (1993) to the case of ductile powder compaction modeling is presented below.

3.2.1. Incremental formulation in the constitutive driver

For a typical finite time step $\Delta t = t_{n+1} - t_n$, one usually applies the Euler backward algorithm to the evolution equations (Box 1) which then transform into the following general discrete evolution equations (Simo, 1992; Simo et al., 1988b):

$$\varepsilon_{n+1} = \varepsilon_n + \Delta\varepsilon_{n+1} \tag{4}$$

$$\varepsilon^{\mathrm{p}}_{n+1} = \varepsilon^{\mathrm{p}}_n + \Delta\varepsilon^{\mathrm{p}}_{n+1} \tag{5}$$

$$k_{n+1} = F(k_n, \Delta\varepsilon^{\mathrm{p}}_{n+1}) \tag{6}$$

with:

$$\Delta\varepsilon^{\mathrm{p}}_{n+1} = \sum_{i=1}^{3} \Delta\lambda_i \partial_\sigma f_i(\sigma, k) \tag{7}$$

where $\Delta\lambda_i$ is the increment of the plastic consistency parameter and where $\Delta\varepsilon^{\mathrm{p}}_{n+1}$ is the tensor of plastic strain increment.

The stress tensor σ_{n+1} can then be deduced from the constitutive relation as

$$\sigma_{n+1} = \overline{\mathbf{C}} : e^{\mathrm{e}}_{n+1} \tag{8}$$

For pressure sensitive yield functions, it is necessary to decompose the involved stress and strain into their spherical and deviatoric parts. For strain increment tensors, we have:

$$\Delta\varepsilon^{\mathrm{p}}_{n+1} = \tfrac{1}{3}(\Delta I^{\mathrm{p}}_1)_{n+1}\mathbf{1} + \Delta e^{\mathrm{p}}_{n+1} \tag{9}$$

$$\Delta\varepsilon_{n+1} = \tfrac{1}{3}(\Delta I_1)_{n+1}\mathbf{1} + \Delta e_{n+1} \tag{10}$$

and for the Cauchy stress tensor, this decomposition can be written as

$$\sigma_{n+1} = \tfrac{1}{3}J_1\mathbf{1} + \mathrm{dev}[\sigma] = \tfrac{1}{3}(J_1)_{n+1}\mathbf{1} + s_{n+1} \tag{11}$$

where $e = \mathrm{dev}[\varepsilon]$, $I_1 = \mathrm{tr}[\varepsilon] = 3\varepsilon_v$ and $s = \mathrm{dev}[\sigma]$, $J_1 = \mathrm{tr}[\sigma] = 3p$ with p being the pressure.

The rest of the process comprises the two main phases: an elastic predictor phase followed by a plastic phase when applicable.

3.2.2. Elastic prediction

In this stage, one assumes that the time step increment is totally elastic, or in other words that the plastic flow is frozen during the step and hence set $\Delta\lambda_{i(n+1)} = 0$. This results in the so called trial state:

$$\varepsilon^{\mathrm{p}}_{n+1}{}^{\mathrm{T}} = \varepsilon^{\mathrm{p}}_n, \quad k^{\mathrm{T}}_{n+1} = k_n, \qquad \text{with } \varepsilon_{n+1} = \varepsilon_n + \Delta\varepsilon_{n+1} \tag{12}$$

Using constitutive equations (Box 1), we can deduce the trial dependent variables. The so called trial stress is defined by (Eq. (13)) which, in terms of its hydrostatic and deviatoric parts, results in Eqs. (14a) and (14b):

$$\sigma^{\mathrm{T}}_{n+1} = \mathbf{C} : \left(\varepsilon_{n+1} - \varepsilon^{\mathrm{p}}_n\right) = \mathbf{C} : \left(\varepsilon^{\mathrm{e}}_n + \Delta\varepsilon_{n+1}\right) = \sigma_n + \mathbf{C} : \Delta\varepsilon_{n+1} \tag{13}$$

$$J^{\mathrm{T}}_{1,n+1} = J_{1,n} + 3K\Delta\varepsilon_{v,n+1} \tag{14a}$$

$$s^{\mathrm{T}}_{n+1} = s_n + 2G\Delta e_{n+1} \tag{14b}$$

If, all of the yield criteria are satisfied for these trial values, i.e. if $f_i(\sigma^{\mathrm{T}}_{n+1}, k^{\mathrm{T}}_{n+1}) \leqslant 0$ for all $i \in (1, \ldots, 3)$ with $(\Delta\lambda_i)^{\mathrm{T}}_{n+1} = 0$, the process is elastic; so the trial values of the state variables in (Eq. (12)) can be accepted as the final values at time t_{n+1}. Otherwise, if $f_\beta(\sigma^{\mathrm{T}}_{n+1}, k^{\mathrm{T}}_{n+1}) > 0$ for some $\beta \in (1, 2, 3)$, the process is plastic and we must enforce the plastic consistency condition by determining the active yield function for which $(\Delta\lambda_\beta)_{n+1} > 0$ (Simo et al., 1988b).

3.2.3. Detection of active mode and plastic correction

One of the difficult task in multisurface plasticity is the accurate determination of the active mode and the transition from one mode to another (singular cases). At each load increment, only one of six possible modes can be active. The trial stress state is used to evaluate a trial value of the different yield functions. If only one yield surface is active (i.e. if for only one $\gamma \in (1,2,3)$, we have $(\Delta\lambda_\gamma)_{n+1} > 0$, then the condition $f_\gamma(\sigma^{\mathrm{T}}_{n+1}, k^{\mathrm{T}}_{n+1}) > 0$ does imply that $(\Delta\lambda_\gamma)_{n+1} > 0$) so that the γ-constraint is active.

However, when several yield surfaces are active, condition $f_\gamma(\sigma^{\mathrm{T}}_{n+1}, k^{\mathrm{T}}_{n+1}) \geqslant 0$ does not imply that $(\Delta\lambda_\gamma)_{n+1} > 0$ since we may have $f_\gamma(\sigma^{\mathrm{T}}_{n+1}, k^{\mathrm{T}}_{n+1}) \geqslant 0$ but $f_\gamma(\sigma_{n+1}, k_{n+1}) < 0$. In that case, a corner mode is concerned and involves the intersection of two yield surfaces.

In addition to the elastic mode and to the three modes related to the three yield surfaces, two singular modes thus result from the nonsmooth intersection of these surfaces (Fig. 1). These are the singular compressive mode (4) and the singular tensile mode (2). A general procedure for determining the active yield surfaces is then based on a systematic enforcement of the discrete Kuhn–Tucker conditions. Using the assumption of the convexity of the yield surfaces, it can be shown (Hofstetter et al. 1993, Simo et al., 1988a) that if all of the trial values of the yield functions are negative, the load is totally elastic and the trial stress state corresponds to the real state:

$$f^{\mathrm{T}}_{i_{n+1}} < 0, \quad \forall i = (1,2,3) \quad \Rightarrow \quad \Delta\lambda_i = 0, \quad \forall i = (1,2,3) \;\; i = (1,2,3) \tag{15}$$

Instead, if one of the trial values of the yield functions is positive, the loading is elastoplastic and one of the plastic modes is necessarily active. In that case, the elastic stress predictor is larger than the real stress state and a plastic correction must be performed. This is done by a correction procedure, also called return mapping algorithm, done by normally projecting the trial stress to the tension, shear and cap surfaces as shown in (Fig. 2) after evaluating the plastic strain increment required to update the stress state:

$$J_{n+1} = J^{\mathrm{T}}_{n+1} - 3K\Delta I^{\mathrm{p}}_{n+1} \tag{16a}$$

$$s_{n+1} = s^{\mathrm{T}}_{n+1} - 2G\left(\Delta e^{\mathrm{p}}_{n+1}\right) \tag{16b}$$

The stress conditions of each one of the plastic modes is presented in Box 2 together with the corresponding values of the increments of plastic consistency parameters. These values are then used to determine the plastic strain increment (Eq. (7)) and thus the real stress state (Eqs. (14a) and (14b)).

It should be noted that the cap mode is the only one involving strain hardening. Therefore, its numerical treatment is more delicate and will be detailed in the next section.

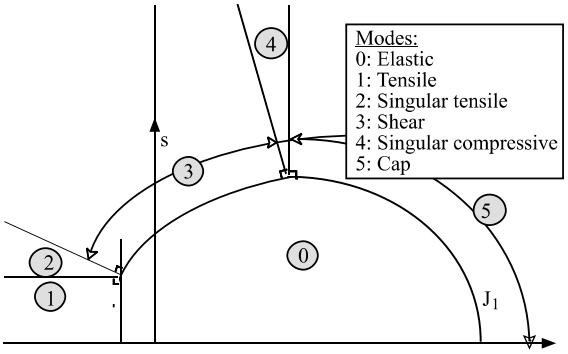

Fig. 1. Different modes of the cap model.

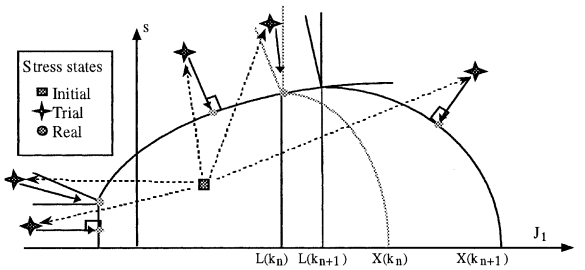

Fig. 2. Closest point projection in the different plastic modes.

Box 2. Boundaries and plastic consistency parameters of the plastic modes.

Mode	Stress state boundaries	Incremental consistency parameters
1	$J^{\mathrm{T}}_{n+1} \leqslant T$ and $s^{\mathrm{T}}_{n+1} \leqslant F_{\mathrm{e}}(T)$	$\Delta\lambda_{1n+1} = \frac{T - J^{\mathrm{T}}_{n+1}}{9K}$, $\Delta\lambda_{2n+1} = 0$ and $\Delta\lambda_{3n+1} = 0$
2	$\begin{cases} J^{\mathrm{T}}_{n+1} \leqslant T \\ F_{\mathrm{e}}(T) < s^{\mathrm{T}}_{n+1} < F_{\mathrm{e}}(T) + \frac{T - J^{\mathrm{T}}_{n+1}}{(\mathrm{d}F_{\mathrm{e}}(T)/\mathrm{d}J)} \end{cases}$	$\Delta\lambda_{1n+1} = \frac{s^{\mathrm{T}}_{n+1} - F_{\mathrm{e}}(T)}{2G}$ $\Delta\lambda_{2_{n+1}} = \frac{T - J^{\mathrm{T}}_{n+1}}{9K} - \frac{\mathrm{d}F_{\mathrm{e}}(T)}{\mathrm{d}J}\frac{s^{\mathrm{T}}_{n+1} - F_{\mathrm{e}}(T)}{2G}$ $\Delta\lambda_3 = 0$
3	$\begin{cases} J^{\mathrm{T}}_{n+1} \leqslant k_n \\ F_{\mathrm{e}}(T) + \frac{T - J^{\mathrm{T}}_{n+1}}{(\mathrm{d}F_{\mathrm{e}}(T)/\mathrm{d}J)} < s^{\mathrm{T}}_{n+1} \\ s^{\mathrm{T}}_{n+1} < F_{\mathrm{e}}(k_n) + \frac{k_n - J^{\mathrm{T}}_{n+1}}{(\mathrm{d}F_{\mathrm{e}}(k_n)/\mathrm{d}J)} \end{cases}$	$\Delta\lambda_1 = 0$, $\Delta\lambda_{2n+1} = \frac{s^{\mathrm{T}}_{n+1} - F_{\mathrm{e}}(J_{n+1})}{2G}$ [J_{n+1} previously obtained by NR solution of the combination of Eqs. (14a) and (14b) and $(f_2(\sigma) = 0)$] $\Delta\lambda_3 = 0$
4	$\begin{cases} J^{\mathrm{T}}_{n+1} \leqslant k_n \\ s^{\mathrm{T}}_{n+1} > F_{\mathrm{e}}(k_n) + \frac{k_n - J^{\mathrm{T}}_{n+1}}{(\mathrm{d}F_{\mathrm{e}}(k_n)/\mathrm{d}J)} \end{cases}$	$\Delta\lambda_1 = 0$ $\Delta\lambda_{2n+1} = \frac{k_n - J^{\mathrm{T}}_{n+1}}{9K(\mathrm{d}F_{\mathrm{e}}(k_n)/\mathrm{d}J)}$ $\Delta\lambda_{3n+1} = \frac{s^{\mathrm{T}}_{n+1} - F_{\mathrm{e}}(k_n)}{2G} - \frac{k_n - J^{\mathrm{T}}_{n+1}}{9K(\mathrm{d}F_{\mathrm{e}}(k_n)/\mathrm{d}J)}$
5	$\begin{cases} L(k_n) < J^{\mathrm{T}}_{n+1} \leqslant X(k_n) \\ s^{\mathrm{T}}_{n+1} > F_{\mathrm{c}}(J^{\mathrm{T}}_{n+1}) \end{cases}$ or $J^{\mathrm{T}}_{n+1} > X(k_n)$	$\Delta\lambda_1 = 0$ $\Delta\lambda_2 = 0$ $\Delta\lambda_{3n+1} = \frac{R^2\Delta I^{\mathrm{p}}_{n+1}F_{\mathrm{c}}(k_{n+1})}{3J^{\mathrm{T}}_{n+1} - 9K\Delta I^{\mathrm{p}}_{n+1} - 3k_{n+1}}$ (see details in cap mode treatment)

3.2.4. Cap mode treatment

As for the other modes, the application of the general flow rule to the function f_3 of the cap mode allows for the determination of the plastic strain increment:

$$\Delta e^{\mathrm{p}}_{n+1} = \Delta\lambda_{3n+1}\frac{s_{n+1}}{F_{\mathrm{c}}(s_{n+1}, J_{n+1}, k_{n+1})} \tag{17a}$$

$$\Delta I^{\mathrm{p}}_{n+1} = 3\Delta\lambda_{3n+1}\frac{J_{n+1} - k_{n+1}}{R^2F_{\mathrm{c}}(s_{n+1}, J_{n+1}, k_{n+1})} \tag{17b}$$

These quantities are then introduced into the relation between trial and real stress states (Eqs. (14a) and (14b)) together with the plastic consistency condition $(f_{3n+1}(\sigma, k) = 0)$. However, since the yield function undergoes hardening that makes the state variable k to attain a new undetermined value k_{n+1}, we thus have an additional unknown. Therefore, in order for the problem to be completely defined, a new relation must

be introduced. This corresponds to the incremental form of the hardening law obtained by an implicit Euler integration scheme between t_n and t_{n+1}:

$$\Delta I^{\mathrm{p}}_{n+1} = W\left(\mathrm{e}^{DX(k_n)} - \mathrm{e}^{DX(k_{n+1})}\right) \tag{18}$$

Thus, the problem is reduced to a single scalar nonlinear equation in k_{n+1} (Eq. (19)) that can be solved by a local Newton–Raphson iterative method. Once this new position of the cap is determined, the plastic strain and the real stress state can be computed (Hofstetter et al. 1993; Simo et al., 1988a).

$$\sqrt{\left[\frac{s^{\mathrm{T}}_{n+1}F_{\mathrm{e}}(k_{n+1})}{F_{\mathrm{e}}(k_{n+1}) + 2G\Delta\lambda_{3_{n+1}}}\right]^2 + \left[\frac{J^{\mathrm{T}}_{n+1} - k_{n+1}}{R + \frac{9K\Delta\lambda_{3_{n+1}}}{RF_{\mathrm{e}}(k_{n+1})}}\right]^2} = F_{\mathrm{e}}(K_{n+1}) \tag{19}$$

3.2.5. Computation of elastoplastic tangent moduli

The last step of the numerical integration of the constitutive evolution equations is concerned with the determination of the algorithmic material contribution of the powder medium to the FE tangent stiffness matrix. This contribution is computed at the integration point level and is called the elastoplastic tangent moduli. In order to preserve a quadratic rate of convergence for the global FE problem, this moduli should be derived from the algorithmic and not from the continuum mechanics formulation (Chtourou et al., 2001; Simo, 1992; Simo and Ortiz, 1985). In fact, this material tangent moduli corresponds to the stress variation caused by an infinitesimal strain variation:

$$\mathbf{H}^{\mathrm{ep}} = \frac{\mathrm{d}\sigma_{n+1}}{\mathrm{d}\varepsilon_{n+1}} \tag{20}$$

It is determined by a simple derivation of the stress strain relation (Eq. (21)). This formulation requires the determination of the plastic strain variation. This can be done through (Eq. (22)) if the active mode involves no strain hardening and through (Eq. (23)) if the active mode is the cap mode. Details of this derivation procedure are given in Appendix A whereas the integration algorithm main steps are summarized in Box 3.

$$\mathrm{d}\sigma_{n+1} = \mathbf{C} : (\mathrm{d}\varepsilon_{n+1} - \mathrm{d}\varepsilon^{\mathrm{p}}_{n+1}) \tag{21}$$

$$\mathrm{d}\varepsilon^{\mathrm{p}}_{n+1} = \sum_i \left[\mathrm{d}(\Delta\lambda_i)\frac{\partial f_i}{\partial\sigma} + \Delta\lambda_i\frac{\partial^2 f_i}{\partial\sigma^2} : \mathrm{d}\sigma\right] \tag{22}$$

$$\mathrm{d}\varepsilon^{\mathrm{p}}_{n+1} = \mathrm{d}(\Delta\lambda_2)\frac{\partial f_i}{\partial\sigma} + \Delta\lambda_2\left(\frac{\partial^2 f_i}{\partial\sigma^2} : \mathrm{d}\sigma + \frac{\partial^2 f_i}{\partial\sigma\,\partial k} : \mathrm{d}k\right) \tag{23}$$

Box 3. Numerical integration algorithm of the cap model.

Step 1: Elastic prediction

Assume plasticity is frozen at the level reached at time t_n and consider the strain increment to be totally elastic, then find a trial stress state: $\sigma^{\mathrm{T}}_{n+1} = \sigma_n + \bar{\mathbf{C}} : \Delta\varepsilon_{n+1}$ using the elasticity tensor $\bar{\mathbf{C}}$.

Step 2: Finding active mode

Use the trial stress state to evaluate the different yield functions and find out the active mode among those shown in Fig. 1.

Step 3: Elastic updating (if elastic mode is detected)

- Set the stress state equal to the trial stress state
- Leave the state variable unchanged
- Set the elastoplastic tangent moduli equal to the elasticity tensor
- Go to step 6

Step 4: Plastic correction (if one of the plastic modes is detected)

- Combine the following conditions in a scalar equation that is nonlinear in the plastic consistency parameter $\Delta\lambda_i$ and solve it by a local Newton–Raphson scheme:
- Stress–trial stress relationship $\sigma_n = \sigma^{\mathrm{T}}_{n+1} - \bar{\mathbf{C}} : \Delta\varepsilon^{\mathrm{p}}_{n+1}$
- Plastic flow rule $\Delta\varepsilon^{\mathrm{p}} = \sum_{i=1,3} \Delta\lambda_i \frac{\partial f_i(\sigma,k)}{\partial\sigma}$
- Hardening rule $\Delta\varepsilon^{\mathrm{p}}_v = f(k)$ (only for the cap mode)
- Consistency condition: $f_i(\sigma,k) = 0$
- Once $\Delta\lambda_i$ is found, compute and update the consistent plastic strain increment, the stress and all other state variables.

Step 5: Compute the resulting consistent algorithmic elastoplastic tangent moduli

Step 6: Return to the main program

4. Integrated simulation module

4.1. Overview

In order to make the simulation of powder compaction an attractive design tool, an integrated simulation module has been developed for axisymmetric applications. A general 3D version is currently under development. This module is mainly intended to facilitate and to automate some of the tedious modeling related tasks. It is composed of the I-Deas Master Series CAD software (SDRC, 1994), the ABAQUS nonlinear FE solver (HKS, 1995b), the ABAQUS-Post post-processing (HKS, 1995a) software and finally IDEQUS (Chtourou et al., 1995a): an in-house developed pre-processing and interfacing program. The module layout, as well as the main functions of its components, is described in Fig. 3.

4.2. Pre-processing

The pre-processing is first performed through I-Deas in which the component geometries are defined and then meshed with four node quadrilateral axisymmetric elements using a semi-automatic mapped pattern. User defined macro functions, implemented into I-Deas, are then used for the selection and the identification of the special boundary regions of the powder cavity and tooling components. As shown in Fig. 4, this essentially consists in the identification of:

- Sets of nodes at the extremity of tooling components, intended for the prescription of boundary conditions of the imposed displacement type.
- Powder cavity element sets at the boundary with tooling components together with tooling component element sets at the boundary with powder cavity intended for the prescription of contact conditions.

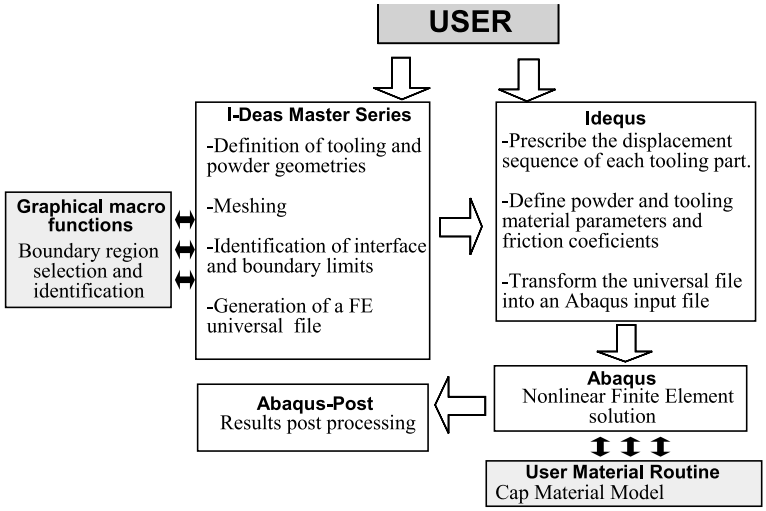

Fig. 3. Integrated simulation module.

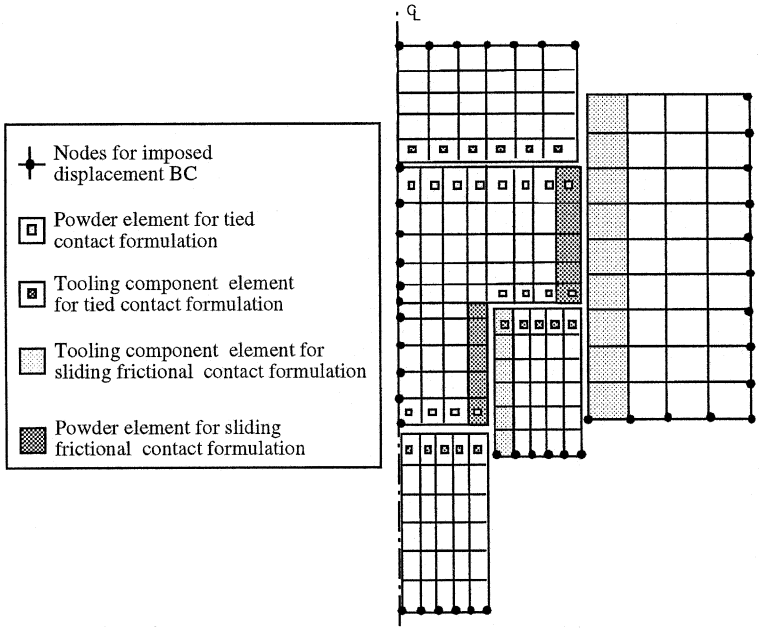

Fig. 4. Boundary regions identified by user developed macro-functions.

Large displacement contact with Coulomb friction was adopted for the interface regions between the powder cavity and tooling component sides. Moreover, since very small powder sliding occurs on punch faces, tied (sticking) contact was adopted for the these interface regions. The friction coefficient was assumed to be equal to 0.2 as in previous studies (Weber and Brown, 1989; Trasorras et al., 1989; Shima and Saleh, 1993) and its reliability was verified by comparing simulated results with experimental measurements as discussed in Section 6. Both contact conditions were modeled using the "master-slave" contact pair

formulation of ABAQUS (HKS, 1995b). This formulation requires the association of the master surface with the stiffer interacting body (tooling component) whereas the slave surface is associated with the second deformable body (powder cavity). IDEQUS automatically identifies, generates and pairs off contact surfaces using the element sets selected by the macro functions.

All the information is written to a universal FE file which is then completed with additional information and then translated into the ABAQUS format by way of the IDEQUS program. This tool also permits to:

- Define powder and tooling material parameters as well as friction coefficients.
- Prescribe the displacement sequence of each tooling component.
- Define the solution control parameters.

4.3. Processing and post-processing

ABAQUS is a FE solver capable of handling both geometric and material nonlinearities, as well as the frictional contact nonlinearities. One of its main advantages is the open facility it offers for the definition of user material models. In fact, the cap material model was implemented into ABAQUS via the UMAT facility that allows the user to define a constitutive model and implement its numerical integration algorithm as a Fortran subroutine (HKS, 1995b). Thus, UMAT is called by the main program at each element integration point within every equilibrium iteration of each load increment of the deformation process. The global FE problem was solved using the classical Newton–Raphson method with a line-search algorithm whereas the local material integration was handled by the closest point projection algorithm (Simo, 1992; Koopman et al., 1992).

Finally, the ABAQUS-Post software (HKS, 1995a) is used mainly for the visualization of the predicted density maps within the compacts. The stress distribution, as well as the deformed shape of the tooling components, could also be post-processed by the same software.

5. Industrial application

5.1. Scope

In this section, a typical compaction case study is presented in order to illustrate the industrial use and to assess the predictive capabilities of the simulation module. The studied part is a three level axisymmetric part, made from the previously characterized 316L stainless steel powder and produced on an industrial basis (Fig. 5). It is compacted in a 250 t hydraulic press using a rigid die and a set of two upper and three lower punches, all made from tool steel.

Since the studied part production started before the simulation module had become operational, the use of this module was not for predictive purposes but for:

- the validation of simulation results;
- and for the investigation of part cracking problems.

First, we start by the simulation of the part compaction as it is performed in the production press. Then, the obtained density distribution is to be validated by comparing it with a second distribution obtained by the developed experimental technique. Finally, in order to solve the part cracking problem, the module is used for investigating the effects of change in the compaction sequence on the density gradient in the compact.

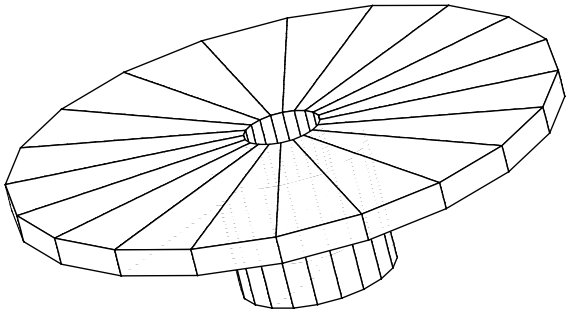

Fig. 5. Part geometry.

5.2. Data modeling

The data set required for the modeling activity includes the tooling geometry, the exact position of each tooling component at each compaction step including the filling and the pressing positions (Fig. 5) and the powder initial density in the cavity. Due to the densification resulting from the automatic press filling, this density is different from the apparent density given by the powder manufacturer. It should be calculated by dividing the final compact mass by the cavity volume. For this application, the initial relative density was 38% whereas apparent density given by the manufacturer was 33%.

As shown in Fig. 6 and Table 1, the first step of the compaction sequence is a powder transfer step, essential to press the lower (inner) level of the part. In order to avoid potential part cracking, any powder transfer operation should be completed prior to any effective compaction step. For this reason, we considered the post-transfer position as the initial modeling position. Thus, the effective compaction sequence consists of two steps.

5.3. Finite element mesh and boundary conditions

The powder initial geometry corresponds to the cavity shape after the powder transfer step whereas the tooling component geometry were simplified since no tooling stress analysis is involved in this study. Moreover, since lower punches 1 and 2 move in unison after powder transfer, they have been modeled as a single punch named "lower punch 1". ABAQUS CAX4 four node axisymmetric element (HKS, 1995b) was used to mesh the geometrical models of the tooling components as well as the powder cavity (Fig. 7).

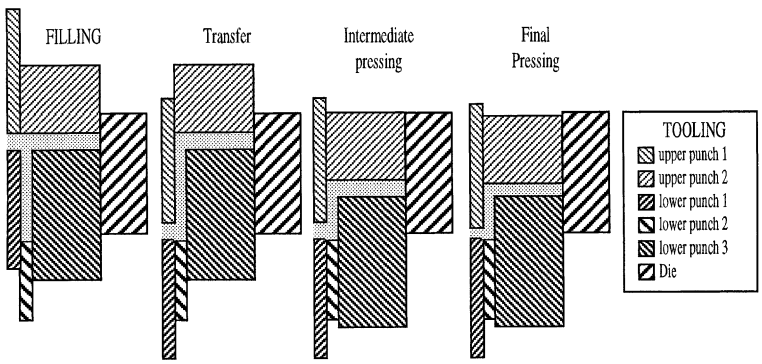

Fig. 6. Tooling and pressing sequence.

Table 1
Tooling positions

Tool	Positions			
	Filling	Transfer	Interm. pressing	Final
Upper punch 1	0	−26.6	−28.5	−28.5
Upper punch 2	0	0	−17.5	−17.5
Lower punch 1	−5	−31.6	−31.6	−31.1
Lower punch 2	−31.6	−31.6	−31.6	−31.1
Lower punch 3	−5.9	−5.9	−18.5	−18.5

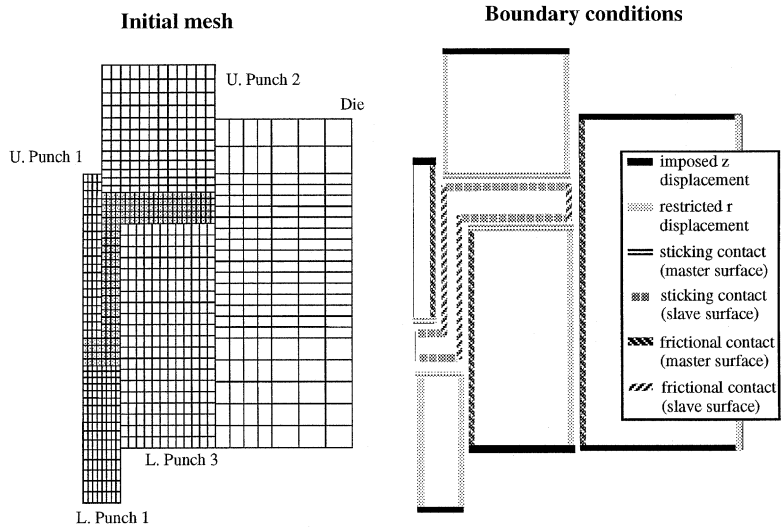

Fig. 7. Initial mesh and boundary conditions of the three-level part.

Ideas user's defined macro functions were implemented and used to identify specific interaction and boundary condition regions. IDEQUS was subsequently used to prescribe the boundary conditions for the analysis steps corresponding to the two sequence compaction steps. The friction coefficient between powder and tool sides was taken to be equal to 0.2 as in previous studies.

5.4. Results

The two-step FE problem was solved by ABAQUS with a relatively small number of increments for each one of the steps. In fact, only four increments were needed for each of the loading steps. In addition, the global Newton–Raphson solution scheme, as well as the local implementation scheme of the cap model, behaves very well. In fact, the number of global equilibrium iterations per increment ranged between 2 and 4. Besides, an average number of 7 local iterations were needed for the material integration algorithm at each global equilibrium iteration. The obtained density distribution is presented in Fig. 8.

In order to validate the simulation results, an experimental density map, presented (Fig. 9), was obtained by the method based on the correlation with Vickers hardness measures. [1] Globally, agreement between

[1] The inner level of the part was too weak to resist during the metallographic preparation procedure.

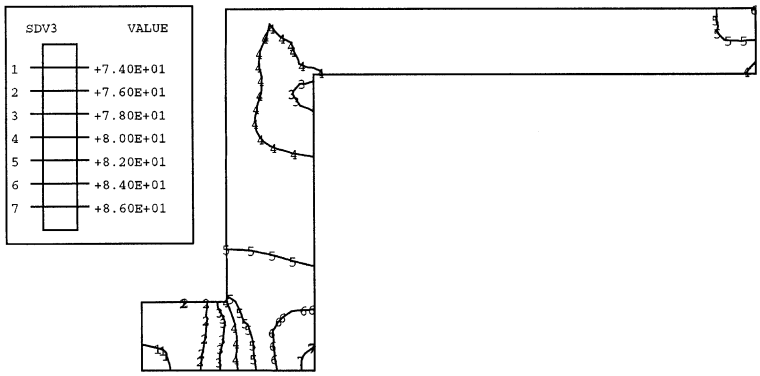

Fig. 8. Final shape and density distribution.

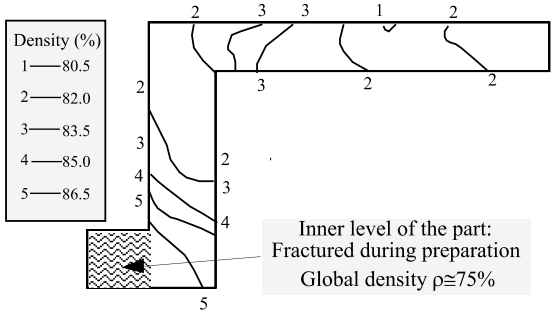

Fig. 9. Experimentally obtained density distribution.

simulated and experimental maps is within the density range of 1%, which is the accuracy of the experimental method (Guillot and Chtourou, 1996). This validation confirmed the high density gradient in the lower region of the part which constitutes a serious quality problem.

5.5. Improving part quality

As may be seen from the simulation and the experimental results, the compaction sequence used for this part led to a huge density gradient in the inner corner region. This gradient is very likely responsible of the noticed part cracking. Part quality could easily be improved by balancing the compaction sequence. This could simply be done by slightly increasing the filling height of the inner level together with an additional compaction of this region using upper punch 1. Furthermore, the compaction sequence could be simplified by using a single step instead of the two-step sequence. This solution was investigated by way of simulation featuring a new compaction sequence (Table 2) leading to the same final dimensions of the compact. Simulation results (Fig. 10) show that this new sequence effectively leads to a more homogeneous and stronger compact. Since results of this figure were intended to illustrate the use of the integrated module in compaction design and not to serve as model validation tests, no corresponding experimental results were obtained.

Table 2
Tooling positions according to the modified compaction sequence

Tool	Positions		
	Filling	Transfer	Final pressing
Upper punch 1	0	−25.6	−29.5
Upper punch 2	0	0	−17.5
Lower punch 1	−6	−31.6	−31.1
Lower punch 2	−31.6	−31.6	−31.1
Lower punch 3	−5.9	−5.9	−18.5

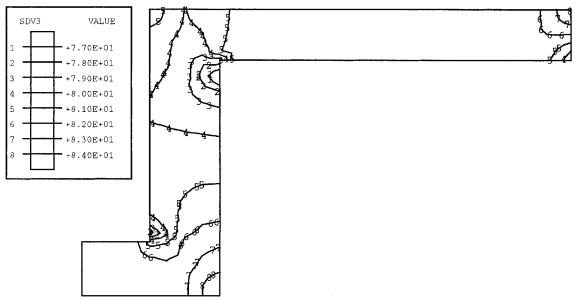

Fig. 10. Simulation results obtained using the modified sequence.

6. Conclusion

In the first (Chtourou et al., 2001) of a series of two papers on PM, the problem of experimental characterization of the material model for the 316L stainless steel powder was addressed together with its experimental validation procedure.

In this second part, computational aspects are addressed based on the FE simulation approach in an integrated simulation environment for industrial application. The problems of rigid die compaction of ductile metal powders involves material, geometric as well as boundary conditions (frictional contact) nonlinearities. While the last two nonlinearities were handled automatically by the ABAQUS FE solver, the first involve a material model unavailable in ABAQUS and hence the elastoplastic cap model had to be formulated and integrated into the software in order to be able to simulate the behavior of the metal powder medium. The closest point projection algorithm was used for the numerical integration of the multisurface plasticity model. Due to its flexibility and capacity to represent all the compaction stages, the cap material model was shown to yield very good results as far as the final density was the main concern and despite the fact that the model was not completely characterized. This is however expectable since the final density is mainly sensitive to the cap hardening parameters which seem to have been correctly identified. Since however no data was available about the shear failure mode the present model parameters cannot correctly simulate the ejection phase and associated residual stresses.

Finally, an integrated simulation environment has been developed and the simulation of the compaction of an industrial PM part has been performed successfully thus demonstrating the practical industrial applications of the computational approach. This application illustrates the modeling activity tasks and demonstrates the accuracy and the numerical efficiency of the implemented computational algorithms.

Further studies are still underway and concern the construction and calibration of a triaxial testing machine aimed at the gathering of the missing data (especially for the failure mode) or incomplete data on elastic behavior at low density levels. Also adjustment of material parameters through optimal parameters identification and inverse modeling process is considered. This will be applied in order to get rid of the current hypothesis of uniform deformation used in extracting material parameter values from the experimental measurements.

Acknowledgements

The authors would like to thank Mr. Sébastien Parent and Ms. Isabelle Jacob from Précitech Inc. for the experimental assistance as well as M. Christian Michaud, Mrs. Cathryn Macrander and M. André Hengartner for their help in software development. The authors would also like to acknowledge the support of the National Sciences and Engineering Research council of Canada (strategic grant no. 0167091 and grant no. CRD-186296).

Appendix A. Derivation of the algorithmically consistent tangent moduli of the cap model [2]

A.1. Case 1: Perfect plasticity

The first variation of the plastic strains is given by

$$\mathrm{d}\varepsilon^{\mathrm{p}}_{n+1} = \sum_i \left[\mathrm{d}(\Delta\lambda_i) \frac{\partial f_i}{\partial \sigma} + \Delta\lambda_i \frac{\partial^2 f_i}{\partial \sigma^2} : \mathrm{d}\sigma \right] \tag{A.1}$$

When combined with Eq. (21) the above relation gives

$$\mathrm{d}\sigma_{n+1} = \Xi : \left(\mathrm{d}\varepsilon_{n+1} - \sum_i \mathrm{d}(\Delta\lambda_i) \frac{\partial f_i}{\partial \sigma} \right) \tag{A.2}$$

where

$$\Xi^{-1} = C^{-1} + \sum_i \Delta\lambda_i \frac{\partial^2 f_i}{\partial \sigma^2} \tag{A.3}$$

This tensor could be inverted numerically or analytically using the Sherman–Morrison method (Hofstetter et al. 1993). This method is privileged since it is numerically cheaper. Furthermore, the plastic consistency parameters $\Delta\lambda_i$ are obtained by use of the normality condition of each of the active yield functions:

$$\mathrm{d}f_i = \frac{\partial f_i}{\partial \sigma} : \mathrm{d}\sigma = 0 \tag{A.4}$$

Using this relation and Eq. (A.3), one can define the following equation system in which $\Delta\lambda_i$ are the unknowns:

$$\sum_i \frac{\partial f_j}{\partial \sigma} : \Xi : \frac{\partial f_i}{\partial \sigma} \mathrm{d}(\Delta\lambda_i) = \frac{\partial f_j}{\partial \sigma} : \Xi : \mathrm{d}\varepsilon \tag{A.5}$$

[2] Subscripts i and j refer to the active yield surfaces.

This system can be more conveniently expressed as follows:

$$\sum_i g_{ji} \mathrm{d}(\Delta\lambda_i) = \frac{\partial f_j}{\partial \sigma} : \Xi : \mathrm{d}\varepsilon \tag{A.6}$$

where

$$g_{ji} = \frac{\partial f_j}{\partial \sigma} : \Xi : \frac{\partial f_i}{\partial \sigma} \tag{A.7}$$

which permits the determination of the plastic consistency parameters:

$$\mathrm{d}(\Delta\lambda_i) = \sum_j g_{ij}^{-1} \left(\frac{\partial f_j}{\partial \sigma} : \Xi : \mathrm{d}\varepsilon \right) \tag{A.8}$$

Finally, the integration of this last relation into Eq. (A.3) we can express the elastoplastic tangent moduli as

$$\frac{\mathrm{d}\sigma_{n+1}}{\mathrm{d}\varepsilon_{n+1}} = \Xi - \sum_i \sum_j g_{ij}^{-1} \left(\Xi : \frac{\partial f_i}{\partial \sigma} \otimes \Xi : \frac{\partial f_j}{\partial \sigma} \right) \tag{A.9}$$

A.2. Case 2: Hardening plasticity (cap mode)

Since the yield function of the cap mode involves the hardening parameter k, the first variation of plastic strains is given by

$$\mathrm{d}\varepsilon^{\mathrm{p}} = \mathrm{d}(\Delta\lambda_3) \frac{\partial f_3}{\partial \sigma} + \Delta\lambda_3 \left(\frac{\partial^2 f_3}{\partial \sigma^2} : \mathrm{d}\sigma + \frac{\partial^2 f_3}{\partial \sigma \, \partial k} : \mathrm{d}k \right) \tag{A.10}$$

Incorporating Eq. (A.10) into Eq. (21), and using the same tensor Ξ defined by Eq. (A.3), one can obtain:

$$\mathrm{d}\sigma = \Xi : \mathrm{d}\varepsilon - \Xi : \frac{\partial f_3}{\partial \sigma} \mathrm{d}(\Delta\lambda_3) - \Delta\lambda_3 \Xi : \frac{\partial^2 f_3}{\partial \sigma \, \partial k} \mathrm{d}k \tag{A.11}$$

In addition, the derivation of cap yield function relatively to its two independent variables gives:

$$\mathrm{d}f_3 = \frac{\partial f_3}{\partial \sigma} : \mathrm{d}\sigma + \frac{\partial f_3}{\partial k} : \mathrm{d}k = 0 \tag{A.12}$$

Furthermore, in order to completely define the problem we should introduce the incremental form of the hardening law (Eq. (A.13)) as well as its derivative (Eq. (A.14)):

$$\frac{1}{3} \Delta I^{\mathrm{p}}(k) - \Delta\lambda_3 \frac{\partial f_3}{\partial J} = 0 \tag{A.13}$$

$$\frac{1}{3} \frac{\mathrm{d}(\Delta I^{\mathrm{p}}(k))}{\mathrm{d}k} \mathrm{d}k - \mathrm{d}(\Delta\lambda_3) \frac{\partial f_3}{\partial J} - \Delta\lambda_3 \times \left(\frac{\partial^2 f_3}{\partial J \, \partial \sigma} : \mathrm{d}\sigma + \frac{\partial^2 f_3}{\partial J \, \partial k} : \mathrm{d}k \right) = 0 \tag{A.14}$$

Finally, this last relation combined with Eq. (A.12) in which Eq. (A.11) is inserted, gives the expression of tangent moduli:

$$\frac{\mathrm{d}\sigma_{n+1}}{\mathrm{d}\varepsilon_{n+1}} = \Xi - \sum_i \sum_j a_{ij}^{-1} \left(\Xi : \frac{\partial f_3}{\partial \sigma} \otimes \Xi : \frac{\partial^2 f_3}{\partial \sigma \, \partial k} \right) \tag{A.15}$$

where subscripts i and j do not refer any more to active yield surfaces but simply takes the values 1 and 2 and where coefficients a_{ij}^{-1} are the components of the inverse of matrix **a** defined by:

$$a_{11} = \frac{\partial f_3}{\partial \sigma} : \Xi : \frac{\partial f_3}{\partial \sigma} \tag{A.16a}$$

$$a_{12} = \frac{\partial f_3}{\partial \sigma} : \Xi : \frac{\partial^2 f_3}{\partial \sigma \partial k} - \frac{1}{\Delta\lambda_3} \frac{\partial f_3}{\partial k} \tag{A.16b}$$

$$a_{21} = \frac{\partial^2 f_3}{\partial \sigma \partial k} : \Xi : \frac{\partial f_3}{\partial \sigma} + \frac{1}{\Delta\lambda_3} \frac{\partial f_3}{\partial J} \tag{A.16c}$$

$$a_{22} = \frac{\partial^2 f_3}{\partial \sigma \partial k} : \Xi : \frac{\partial^2 f_3}{\partial \sigma \partial k} + \frac{1}{\Delta\lambda_3} \frac{\partial^2 f_3}{\partial J \partial k} - \frac{1}{3\Delta\lambda_3^2} \frac{\partial(\Delta I^{\mathrm{p}}(k))}{\partial k} \tag{A.16d}$$

References

Bockstiegel, G., 1968. Relations between pore structures and densification mechanisms in the compacting of iron powder. Perspectives in Powder Metallurgy 3, 54–71.

Chorin, A., Hughes, T.J.R., McCracken, M.F., Marsden, J.E., 1978. Product formulas and numerical algorithms. Communications on Pure and Applied Mathematics 31, 205–256.

Chtourou, H., Gakwaya, A., Guillot, M., Hrairi, M., 1995a. Implementing a cap material model for the simulation of metal powder compaction. Net Shape Processing of Powder Materials, AMD-vol. 216, ASME, San Fransisco, CA, pp. 19–27.

Chtourou, H., Guillot, M., Gakwaya, A., 1995b. Modeling the rigid die compaction of 316L stainless steel powder. Advances in Powder Metallurgy and Particular Materials, Seattle, vol. 1 (part 2), pp. 169–183.

Chtourou, H., Gakwaya, A., Guillot, M., Hrairi, M., 1996. Finite element simulation of the rigid die compaction of metal powder components. Proceedings of the Canadian Society of Mechanical Engineers Forum. McMaster University.

Chtourou, H., Guillot, M., Gakwaya, A., 2001. Modeling of the metal powder compaction process using the cap model. Part I. Experimental material characterization and validation. International Journal of Solids and Structures 39 (4), 1059–1075.

Crawford, J., Lindskog, P., 1983. Constitutive equations and their role in the modeling of the cold pressing process. Scandinavian Journal of Metallurgy 12, 271–281.

Dhatt, G.S., Touzot, G., 1984. In: Maloine, S.A. (Ed.), Une présentation de la Méthode des éléments finis.

Dimaggio, F., Sandler, I., 1971. Material models for granular soils. Journal of the Engineering Mechanics Division, ASCE, vol. 97, pp. 935–950.

German, R.M., 1984. Powder Metallurgy Science. MPIF, Princeton, NJ.

Guillot, M., Chtourou, H., 1996. Generalization of the Vickers hardness local density measurement technique to different powder materials. In: Proceedings of the World Congress on Powder Metallurgy and Particulate Materials, Washington, DC, vol. 1 (part 4), pp. 31–40.

Gurson, A.L., Posteraro, R.A., 1992. Yield functions for metal powders for use in the numerical simulation of powder compaction. TMS Conference, San Diego, CA.

HKS Inc., 1995a. ABAQUS-Post User Guide, Version 5.4. Hibbit, Karlsson and Sorensen, Inc., Rhode Island.

HKS Inc., 1995b. ABAQUS Theory Manual, Version 5.4. Hibbit, Karlsson and Sorensen, Inc., Rhode Island.

Hofstetter, G., Simo, J.C., Taylor, R.L., 1993. A modified cap model: closest point solution algorithms. Computers and Structures 46 (2), 203–214.

Koopman, M.G., Rachakonda, V.B.S., Gurson, A.L., McCabe, T., 1992. Material models for the finite element simulation of compaction of metal powder. TMS Fall Meeting, Chicago.

Kröner, E., 1960. Archive for Rational Mechanics and Analysis 4, 273.

Lee, E.H., Liu, D.T., 1967. Finite strain elastic–plastic theory with application to plane waves analysis. Journal of Applied Physics 38, 19–27.

Lenel, F.V., 1980. Powder Metallurgy, Principles And Applications. MPIF, Princeton, NJ.

Mandel, J., 1971. Plasticité classique et viscoplasticité CISM no. 97 Udine, Springer, Vienna.

Peric, D., Owen, D.R.J., Honnor, M.E., 1992. A model for finite strain elasto-plasticity based on logarithmic strains: computational issues. Computer Methods in Applied Mechanics and Engineering 94, 35–61.

Sandler, I.S., Rubin, D., 1979. An algorithm and a modular subroutine for the cap model. International Journal for Numerical and Analytical Methods in Geomechanics 3, 173–186.

SDRC Corporation, 1994. Ideas Master Series Student Guide.

Shima, S., Saleh, M.A.E., 1993. Variation of density distribution in compacts in closed die compaction with powder characteristics. Advances in Powder Metallurgy and Particulate Materials 3, 175–189.

Simo, J.C., 1992. Algorithms for static and dynamic multiplicative plasticity that preserve the classical return maping schemes of the infinitesimal theory. Computer Methods in Applied Mechanics and Engineering 99, 62–112.

Simo, J.C., Ortiz, M., 1985. A unified approach to finite deformation elastoplasticity based on the use of hyperelastic constitutive equations. Computer Methods in Applied Mechanics and Engineering 49, 222–245.

Simo, J.C., Ju, J.W., Pister, K.S., Taylor, R.L., 1988a. Assessment of cap model: consistent return algorithms and rate dependent extension. ASCE Journal of Engineering Materials 114 (2), 191–218.

Simo, J.C., Kennedy, J.G., Govindje, S., 1988b. Non-smooth multisurface plasticity and viscoplasticity. Loading/unloading conditions and numerical algorithms. International Journal for Numerical Methods in Engineering 26, 2161–2185.

Trasorras, J., Krauss, T.M., Fergusson, B.L., 1989. Modeling the powder compaction using the finite element method. In: Proceedings of the 1989 International Conference on Powder Metallurgy, San Diego, CA, pp. 85–104.

Weber, G.G., Brown, S.B., 1989. Simulation of the compaction of powder components. Advances in Powder Metallurgy and Particulate Materials 1, 105–118.